



Microstructural evolution during high temperature dwell-fatigue of austenitic stainless steels

Hugo Wärner^{a,*}, Jinghao Xu^a, Guocai Chai^{a,b}, Johan Moverare^a, Mattias Calmunger^a

^a Department of Management and Engineering, Linköping University, 58183 Linköping, Sweden

^b AB Sandvik Materials Technology R and D Center, 81181 Sandviken, Sweden

ARTICLE INFO

Keywords:

Creep-fatigue interaction
High temperature austenitic alloys
High-resolution microscopy
Dynamic recrystallization of crack tip plastic zone

ABSTRACT

Microstructural evolution related to the mechanical response from isothermal dwell-fatigue testing at 700 °C of two austenitic steels, Eshete 1250 and Sanicro 25, is reported. Coherent Cu-precipitates and incoherent Nb-carbides were found to impede dislocation motion, increase hardening and improving the high temperature properties of Sanicro 25. Sparsely placed intergranular Cr- and Nb-carbides made Eshete 1250 susceptible to creep damage and intergranular crack propagation, mainly from interaction of the carbides and fatigue induced slip bands. Dynamic recrystallization of the plastic zone at the crack tip appeared to affect crack propagation of Sanicro 25 by providing an energetically privileged path.

1. Introduction

Flexible generation of power is critical to compensate for the deficiencies of renewable power generation, such as solar and wind power, which is bound to increase the number of start-and-stop cycles in future power plants [1–3]. These operating conditions contribute to a combined accumulation of cyclic fatigue damage and time-dependent creep damage originating from thermal transients during start-up and shut-down and stresses during operation. The interaction behaviour of creep and fatigue of a boiler material is complex and can be an individual, a competing or an additive process [4,5]. Traditionally, ferritic and austenitic stainless steels are used for critical components of power plants. However, recent studies indicate that highly alloyed austenitic stainless steels could be the more suitable candidates for long-term service with these more demanding operating conditions [6]. Ogata and Arai [7] investigated two commonly used boiler materials, the austenitic stainless steels SUS304 and 316FR, and reported that they showed creep and creep-fatigue (CF) interaction damage in their microstructures after high temperature cycling. Prior creep damage did not affect the subsequent fatigue damaging process, it only accelerated the creep damaging mechanisms i.e. the interlinking between the transgranular fatigue cracks and the creep-initiated cavities was not enhanced by creep pre-loading. Hales [8] presented four principal cases of creep-fatigue interaction damage based on the austenitic stainless steel AISI 316: (1) Transgranular 100% fatigue driven cracking, (2)

transgranular competing propagation where both fatigue and creep obey their own separated failure criteria (no interaction), (3) mixed interaction where transgranular fatigue driven cracks interlink with creep-initiated cavities and (4) intergranular 100% creep driven propagation. Illustrations of these cases can be seen in Fig. 1. Later these principal layouts were extended by Plumbridge [4] and expanded the concept with the additive, competitive and interactive cases. The different cases have been incorporated into damage interaction diagrams which feature in many high temperature code cases (ASME, R5, RCC-MR etc.), which typical methodology is to assess the damage formation when both fatigue and creep mechanisms operate. Test data is plotted as creep life fraction and fatigue life fraction and by drawing lower bound lines to the data inputs, the parameters for safe design can be computed [9]. For the austenitic stainless steels Sanicro 25 and Eshete 1250 such a diagram was generated and evaluated using the principal cases of Hales [8] and Plumbridge [4], in a previous publication by Wärner et al. [10], but no microstructural investigations were considered. In that study it was found that both materials suffered from creep-fatigue interaction damage that limited the amount of cycles to failure, Eshete 1250 showed more creep elongation and Sanicro 25 suffered higher maximum stresses but in general still showed superior CF life compared to Eshete 1250. Other studies have also investigated the high temperature properties of Sanicro 25 in terms of low cycle fatigue (LCF), thermomechanical fatigue (TMF) and creep and they report high initial hardening rate (due to nano sized precipitates), stable

* Corresponding author.

E-mail address: hugo.warner@liu.se (H. Wärner).

<https://doi.org/10.1016/j.ijfatigue.2020.105990>

Received 8 July 2020; Received in revised form 4 October 2020; Accepted 8 October 2020

Available online 13 October 2020

0142-1123/© 2020 The Author(s). Published by Elsevier Ltd. This is an open access article under the CC BY license (<http://creativecommons.org/licenses/by/4.0/>).

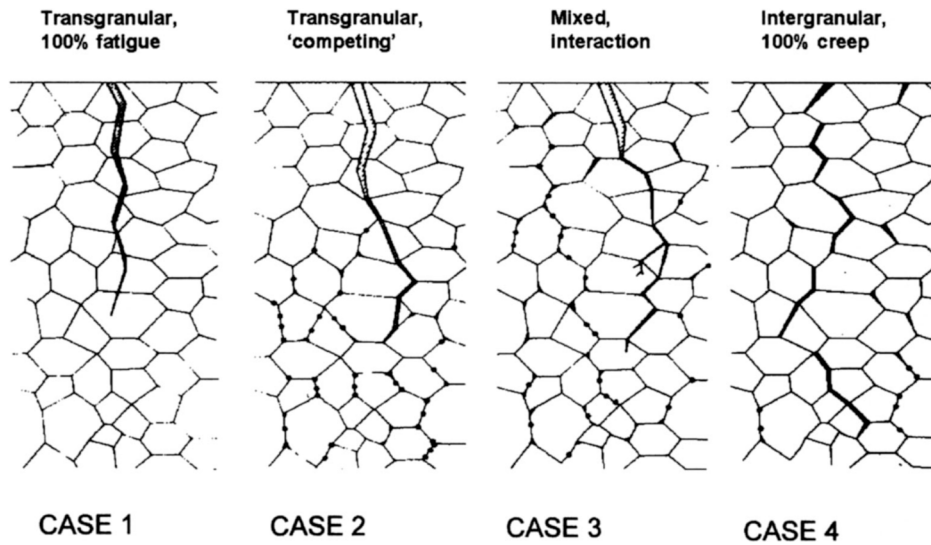


Fig. 1. Different cases of creep-fatigue interaction damage according to Hales [8] (Courtesy of publisher).

Table 1

Chemical composition (in wt%) of the austenitic alloys.

Material	C	Cr	Ni	W	Co	Cu	Mn	Nb	N	Si	V	Mo	Fe
Sanicro 25	0.1	22.5	25.0	3.6	1.5	3.0	0.5	0.5	0.23	0.2	–	–	Bal.
Esshete 1250	0.1	15	9.5	–	–	–	6.3	1.0	–	0.5	0.3	1.0	Bal.

microstructural evolution, very good creep and LCF properties compared to other austenitic stainless steels e.g. the medium alloyed Esshete 1250 [11–14]. Reportedly Esshete 1250 is strengthened by homogeneous dispersed MX (Nb-rich) particles of various sizes and was developed for withstanding high temperature creep loadings [15].

This paper presents a microstructural investigation of two austenitic stainless steels, that are candidates for critical components in the power generation industry. The investigations were performed after the specimens had been exposed to high temperature isothermal dwell-fatigue in order to determine the creep-fatigue interaction behaviour and damage mechanisms. The mechanical response has partly been evaluated in a previous study [10].

2. Materials and methods

The materials considered for this study were Sandvik Sanicro 25 (solution heat-treated at 1220 °C for 10 min) and Esshete 1250 (solution heat-treated at 1100 °C for 15 min). Sanicro 25 had an average initial grain size of ASTM 3.8 (average diameter of 26.9 μm , but larger grains up to 150 μm were seen in the microstructure) and Esshete 1250 had an average initial grain size of ASTM 4.3 (average diameter of 21.6 μm , but larger grains up to 100 μm were seen in the microstructure). The chemical compositions of the investigated materials in wt% can be

viewed in Table 1. Specimens of the materials, processed according to Fig. 2, were subjected to isothermal dwell-fatigue testing at 700 °C as shown in Fig. 3, with strain controlled cyclic part (black dotted line) and load controlled dwell part (black solid line). All the evaluated conditions from [10] can be viewed in Table 2. The number of cycles to failure (N_f) was defined as the point where the maximum stress range ($\Delta\sigma$) decreases 10%, as specified in [16]. More details regarding the dwell-fatigue experiment are given in [10].

Longitudinal cross sections of the tested specimens were ground and polished following the procedure used in [11]. The microstructural investigations were performed with a HITACHI SU-70 field emission gun (FEG)-scanning electron microscope (SEM) equipped with a solid-state backscattered electron (BSE) detector, using 10–20 kV acceleration voltage and working distances between 7 mm and 20 mm. The analysis techniques used were electron backscatter diffraction (EBSD), energy-dispersive spectroscopy (EDS) and wavelength-dispersive spectroscopy (WDS). Scanning transmission electron microscopy (STEM) were used to investigate deformation substructures and nano sized precipitates of

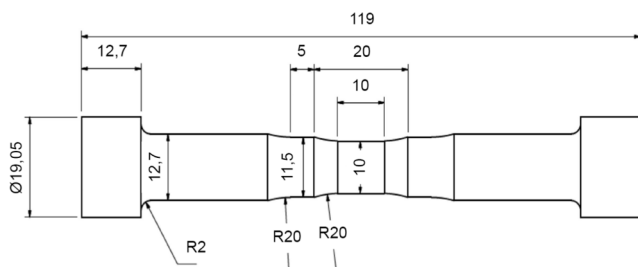


Fig. 2. Schematics of the test specimen (units in millimetres).

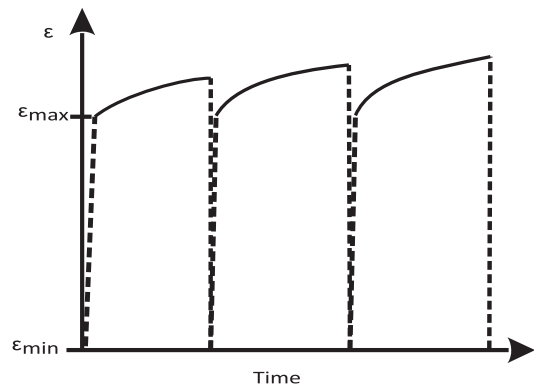


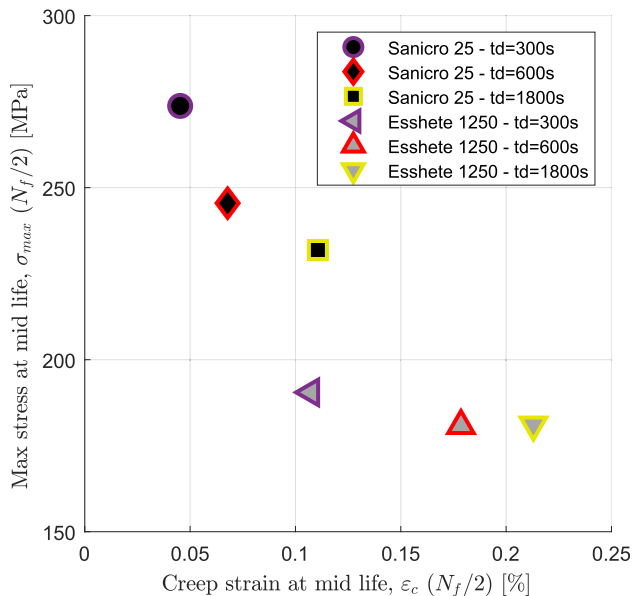
Fig. 3. Sketch of the dwell-fatigue test cycle. The solid lines represents the load controlled parts and the dotted lines represents the strain controlled parts.

Table 2

Dwell-fatigue conditions of the investigated specimens [10].

Material	$\Delta\epsilon/2$ [%]	Dwell time, t_d [s]	Temperature [$^{\circ}$ C]
Sanicro 25	0.25	300	700
Sanicro 25	0.25	600	700
Sanicro 25	0.25	1800	700
Esshete 1250	0.25	300	700
Esshete 1250	0.25	600	700
Esshete 1250	0.25	1800	700

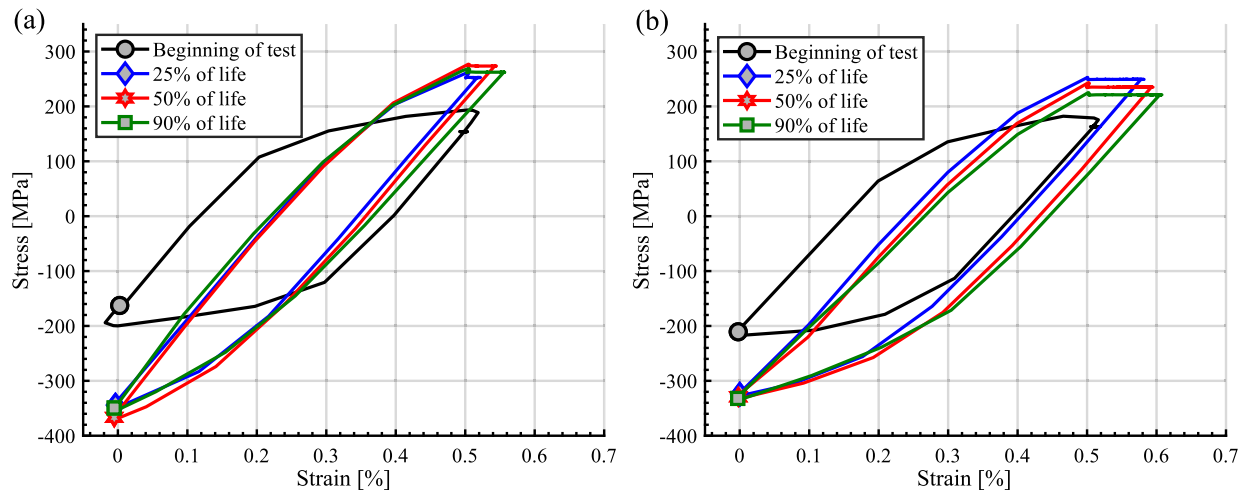
thin foils prepared from the gauge section of the tested specimens. The TEM samples were ground to 60 μ m and then punched into 3 mm discs. Twin-jet electro-polishing was conducted with an electrolyte solution containing 10% perchloric acid and 90% ethanol, using a polishing temperature of -25° C. The STEM investigation was performed by a FEI Tecnai G2 microscope operated at 200 kV. Images were captured using different camera lengths: high angle annular dark field images were obtained with a camera length of 140 mm, dark field with 350 mm and bright field with 2100 mm.

**Fig. 4.** Mechanical response of the investigated conditions, $\Delta\epsilon/2 = 0.25\%$ [10].

3. Results

Previous studies that have investigated the mechanical response during high temperature dwell-fatigue conditions agree that the susceptibility for creep and the interaction of creep and fatigue are found to be the most important life limiting properties [10,12,13,17]. The dwell-fatigue performance focusing on the creep resistance during the dwell time of the two investigated materials are summarised in Fig. 4. Clearly there is a difference in creep resistance of the two materials where the creep strain (referring to the accumulated strain during the constant load part (solid line) in Fig. 3) at mid life, $\epsilon_c (N_f/2)$, are lower for the Sanicro 25 tests, although the maximum stresses at mid life, $\sigma_{max} (N_f/2)$, are higher than for equivalent Esshete 1250 tests. The hysteresis curves in Fig. 5 and Fig. 6 show the evolution of the plastic response and the creep straining for both material test extremes, i.e. the tests with the shortest and the longest dwell time, t_d . Fig. 5 (a-b) both show prominent hardening, from the beginning of the test to 25% of the CF life for the two Sanicro 25 test conditions. As indicated in Fig. 4, the maximum stress of the $t_d = 1800$ s test, is generally lower due to increased creep damage during the longer dwell time. During the CF life the Esshete 1250 test extremes both show increasing plastic strain range, $\Delta\epsilon_p$, as shown by Fig. 6(a-b). Compared to the Sanicro 25 tests, the hardening in the first CF life quarters is not as prominent. As can be seen in Fig. 4, longer t_d yield increased $\epsilon_c (N_f/2)$, for both materials.

In Fig. 7 the microstructure of a Sanicro 25 test with the longest dwell time can be seen. From the crack overview in Fig. 7a, the crack path is highly branched and interconnected with secondary cracks. In Fig. 7b intergranular cavities can be observed in the region close to the transgranular crack path. Due to the existence of those grain boundary cavities, the transgranular crack path was perturbed and turned intergranular. In addition, the EBSD analysis in Fig. 7c shows that the behaviour of the crack paths are most irregular, alternating between transgranular and intergranular and the sites indicated in the figure shows the creep-initiated grain boundary cavity sites. These sites are also commonly associated with areas of smaller average grain sizes. The microstructures of the Sanicro 25 $t_d=600$ s test, Fig. 8, also show similar characteristics and with high plasticity in the vicinity of the cracks, even though the branching is not as appreciable. In Fig. 8a the magnified highly plasticised area, show recrystallized grains at the vicinity of the crack path, where fully recrystallized grains are indicated by blue, highly deformed structures are indicated by red and low deformation level structures are indicated by yellow (RX-image). Fig. 8b show transgranular crack interaction with areas of creep initiated damage, but these are less numerous compared to the $t_d=1800$ s test. The reduced accumulation of life limiting creep-fatigue interaction damage is

**Fig. 5.** Hysteresis curves of Sanicro 25; (a) $t_d = 300$ s, (b) $t_d = 1800$ s [10].

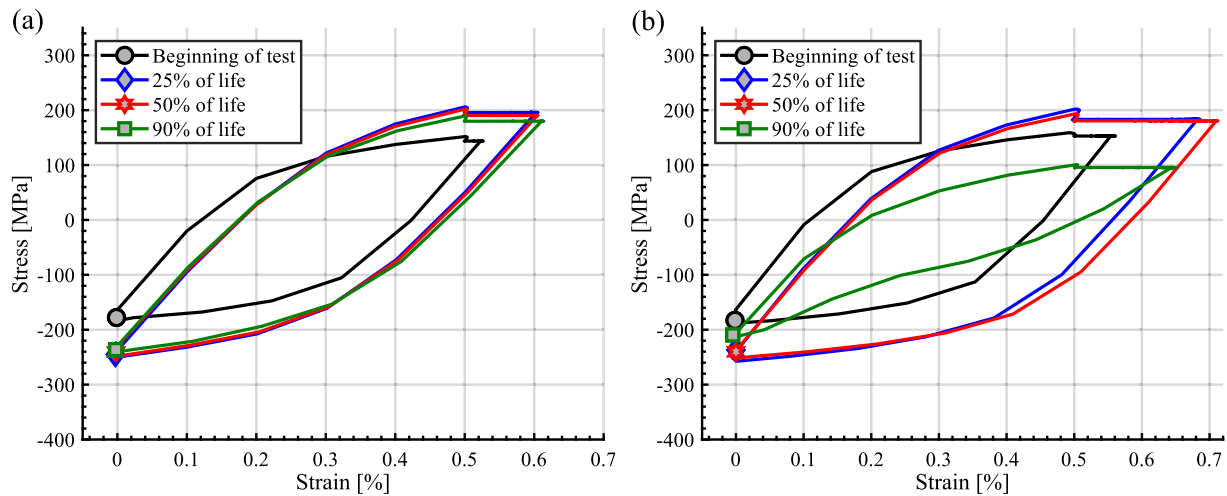


Fig. 6. Hysteresis curves of Esshete 1250; (a) $t_d = 300$ s, (b) $t_d = 1800$ s [10].

therefore attributed to the decreased amount of possibilities for the fatigue driven crack path to link up with the creep-initiated grain boundary cavities. Precipitates and dislocation structures can be seen in Fig. 9 and Fig. 10. The EDS analysis in Fig. 9a show increased amount of chromium, nitrogen, copper and niobium and the pattern of the analysis indicates that there are most likely Z-phase (CrNbN), Nb-carbides and copper-rich precipitates located around and on the grain boundaries. There are also numerous small black circular spots that do not show any elemental enrichment and are most probably holes of removed precipitates due to etching of the TEM-sample. The dislocation structure and pile up close to a grain boundary are presented in Fig. 9b where the increase in dislocation density close to the grain boundary can be seen. In addition, there are Nb- and Cr-carbides in roughly 100 nm-scale in the interior of the grain. In Fig. 10, close up images of the deformation

structure show very small precipitates that interact with the dislocation arrangements. From EDS-analysis these precipitates are identified as Cr-carbides shown in Fig. 10a, a, Nb-carbides shown in Fig. 10b) and copper-rich precipitates shown in Fig. 10b.

The Esshete 1250 tests also showed increased accumulation of ϵ_c ($N_f/2$) with increasing dwell time and as mentioned before, all these tests show higher ϵ_c ($N_f/2$) compared to the equivalent Sanicro 25 tests. By analysing the micrographs of the tests with $t_d=600$ s and $t_d=1800$ s (Fig. 11 and Fig. 12(a-c)) it is obvious that the crack propagation is associated with damage in the grain boundaries. In both cases, there are evidence of regions containing high density of planar slip bands (Fig. 11a and 12a) which interact with the grain boundaries and the local residing precipitates, this can be seen in Fig. 13b) and Fig. 14b. According to the WDS analysis, presented in Fig. 11c and the STEM EDS-analysis, presented in Fig. 14b the precipitates in the grain boundaries and in the grain interiors would be Cr- and Nb-carbides. In Fig. 14a there are evidence of dislocation pinning Nb-carbide and holes originating from ground out precipitates. In contrast to the Sanicro 25 tests, formation of recrystallised grains in the crack tip plastic zone seems to be negligible, as indicated by Fig. 12d.

For the tests with shortest dwell time, $t_d=300$ s, linkage of the fatigue initiated cracks with the creep-initiated grain boundary cavities are less likely, but the same crack characteristics as for the longer t_d tests is still observed according to the Sanicro 25 microstructure, as shown in the overview image Fig. 15a and the EBSD map of Fig. 15b. This contributes to overall reduced dwell-fatigue damage. For Esshete 1250, the fatigue dominated damage contributes less to the overall damage of the precipitated grain boundaries. However as shown in Fig. 16b, the crack path is still intergranular and similarly to the other Esshete 1250 tests this is because of the slipband interaction with the grain boundary precipitates, which is visible in the overview image Fig. 16a.

4. Discussion

On a nanoscale, the microstructures of both the investigated materials contains Nb-carbides that interfere with the movement of dislocations during plastic deformation and increase the strength of the materials at high temperatures. As can be seen in the micrographs, they appear in different configurations and for Sanicro 25 they are commonly positioned at the dislocation lines, as evident in Fig. 10, but they also appear heterogeneous distributed throughout the matrix most likely due to detachment of the dislocation lines during cyclic straining. This has also been reported by Heczko et al. [18] where Nb-carbide nucleation and dislocation detachment continuously occur during high temperature cyclic deformation, which increase the density of incoherent Nb-

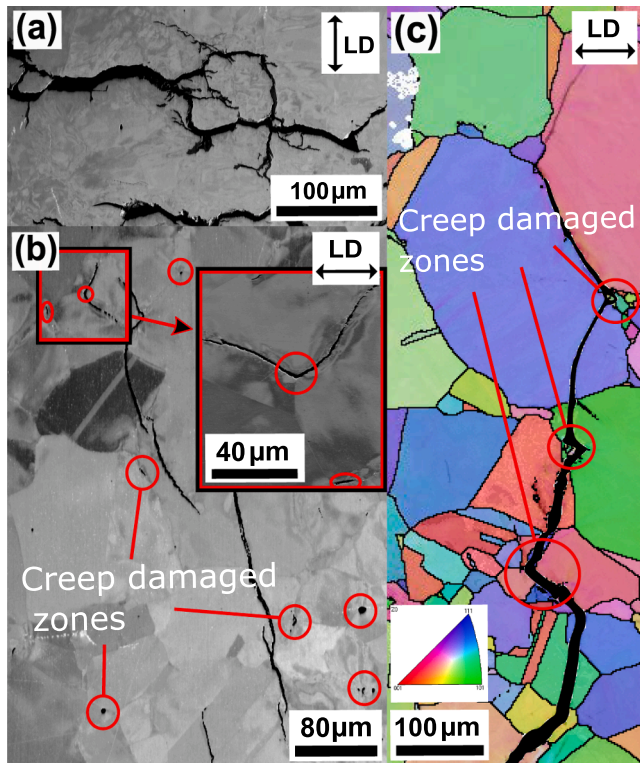


Fig. 7. Crack overview of Sanicro 25, $t_d = 1800$ s; (a) middle of the crack path, (b) and (c) at the end of the crack path.

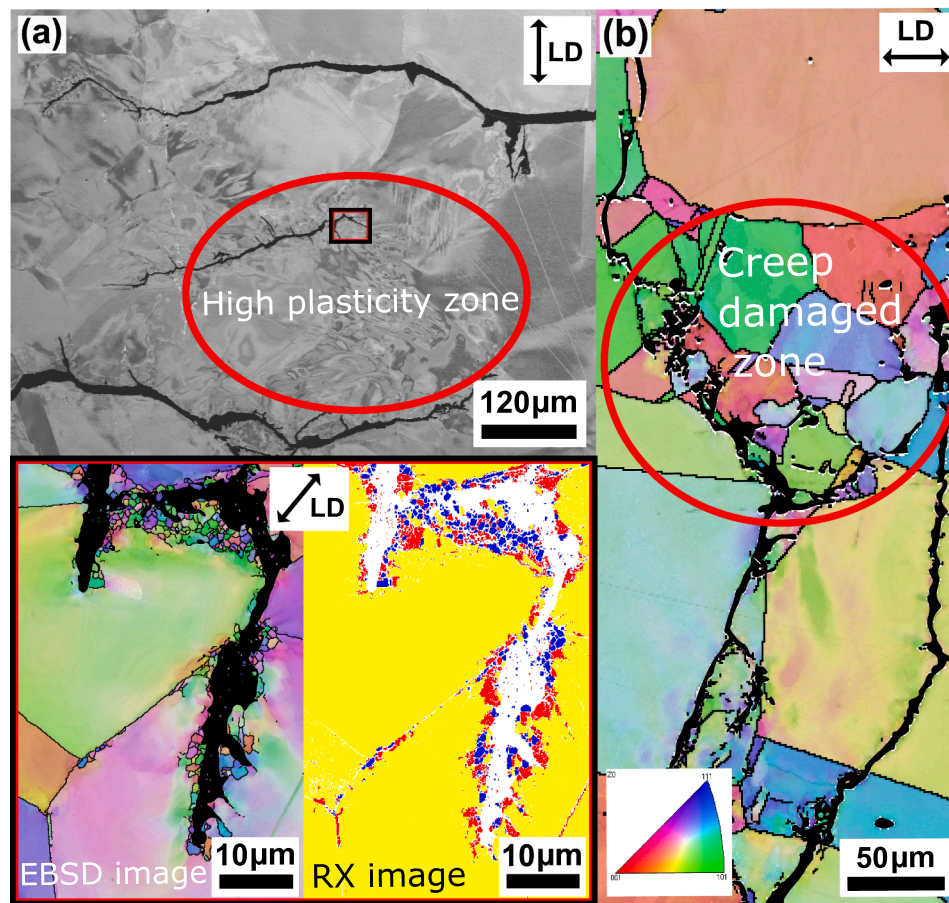


Fig. 8. Crack overview of Sanicro 25, $t_d = 600$ s; (a) overview of the crack path, with EBSD and recrystallized fraction analysis of a zoomed in area of a highly plasticised zone containing a crack tip, (b) at the end of the crack path.

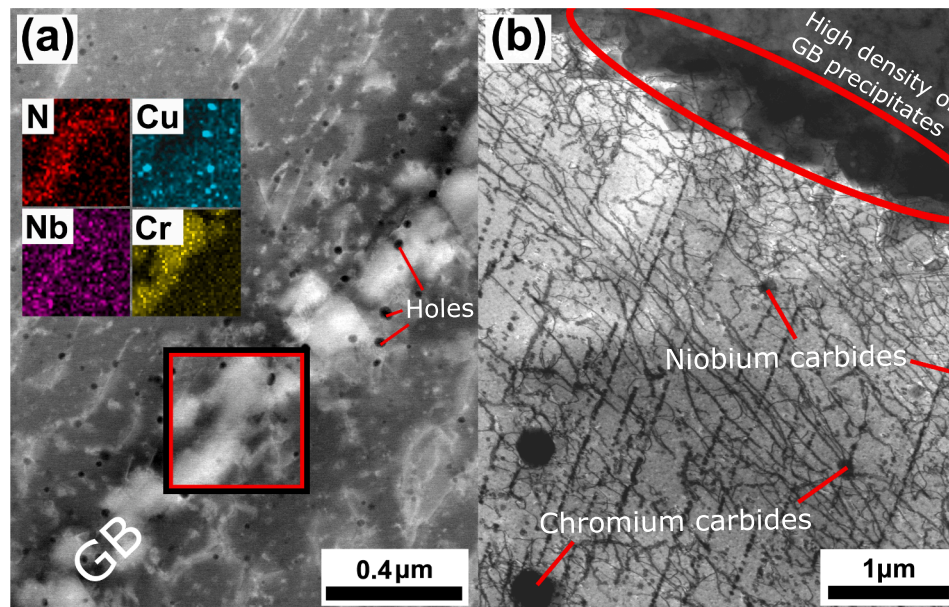


Fig. 9. Dislocation structure and grain boundary precipitates of Sanicro 25, $t_d = 600$ s; (a) STEM dark field imaging and EDS-analysis of grain boundary precipitates, (b) STEM bright field imaging of dislocation structures and dislocation pile ups in the vicinity of a grain boundary.

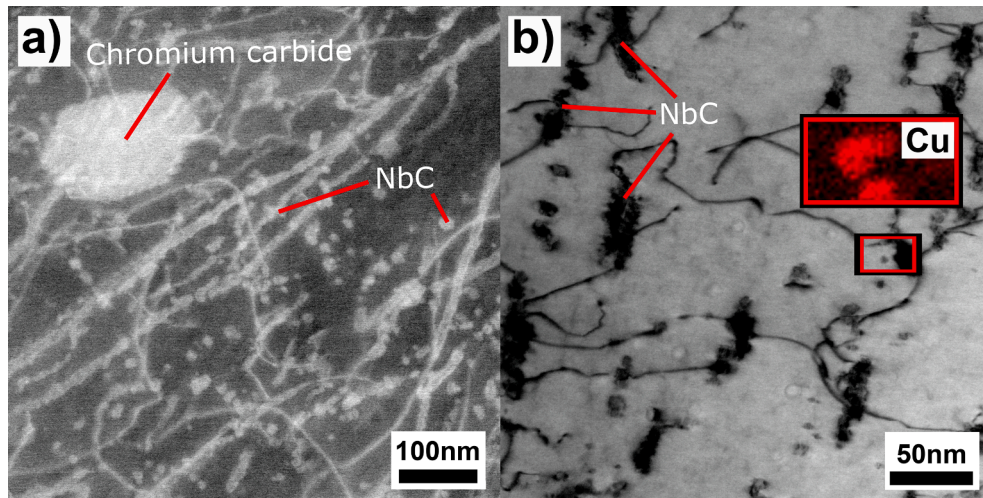


Fig. 10. Dislocation and precipitate interaction at nanometre scale of Sanicro 25, $t_d = 600$ s; (a) STEM dark field imaging, (b) STEM bright field imaging and EDS-analysis.

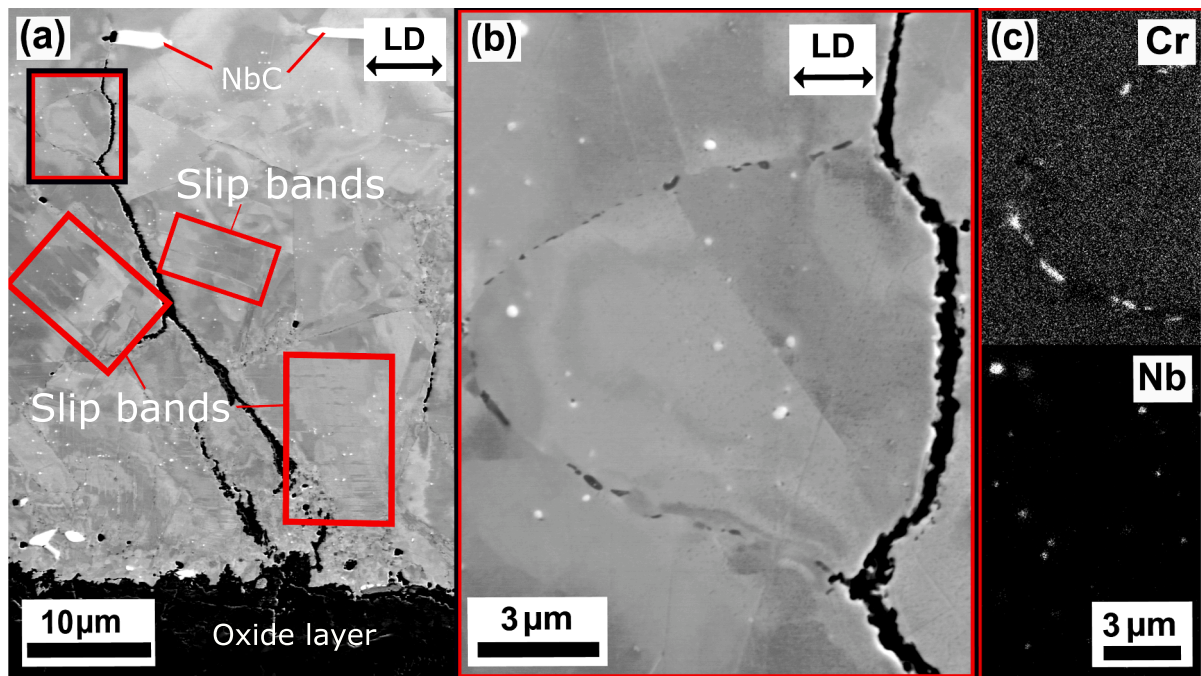


Fig. 11. Crack overview at the specimen surface of Esshete 1250, $t_d = 1800$ s; (a) crack path overview, (b) zoomed in area in (a), (c) WDS-mapping of (b).

carbide obstacles that promotes a hardening effect. In addition, the evidence of Cr-carbides at 100 nm-scale and coherent copper-rich precipitates (Fig. 9 and Fig. 10) contributes to impeding of dislocation movement [13,18] and therefore also add to the hardening effect. These mechanisms ought to elucidate the mechanical response of the Sanicro 25 tests in Fig. 5(a-b). Similar effect of formation and nucleation of Nb-carbides seems to be present in the Esshete 1250 microstructure. However, the grain boundaries have generally lower density of strengthening precipitates compared to Sanicro 25 and instead they contain sparsely spaced Cr-carbides and Nb-carbides, which result in the lower resistance to creep damage, owing to the higher grain-boundary cracking susceptibility [15,19,20]. This can be explained by considering the planar slip bands interaction with the grain boundaries and the local residing precipitates (Fig. 13b) and Fig. 14b) which contributes to debonding of the hard precipitates on the grain boundaries. Furthermore, dislocation pile ups at intersections of slip planes and grain boundaries cause grain

boundary voids (slip voids) and grain boundary sliding leading to fracture of brittle grain boundary Cr-carbides that generate cavities. These concurrent damage mechanisms have also been observed and evaluated by Manson et al. [17], Bayerschen et al. [21] and Calmunger et al. [22]. Because of these active damage mechanisms during the different dwell-fatigue loadings of Esshete 1250, fracture solely occurs along the grain boundaries, while the interior of the grains experience high plasticity in the form of pronounced slip band movement. This explains the comparatively high and increasing plastic strain range, $\Delta\epsilon_p$, shown in both cases of Fig. 6. Consulting the interaction diagram of Esshete 1250 from [10] there should be some evidence of interactive damage lowering the overall cyclic life for these loadings. However, the principal interaction cases proposed by Hales [8], presented in Fig. 1, suggests that the Esshete 1250 dwell-fatigue tests, which have a substantial fatigue portion, are 100% creep dominated. This is based on the macroscopic overview of the crack propagation, but in the case of Esshete 1250

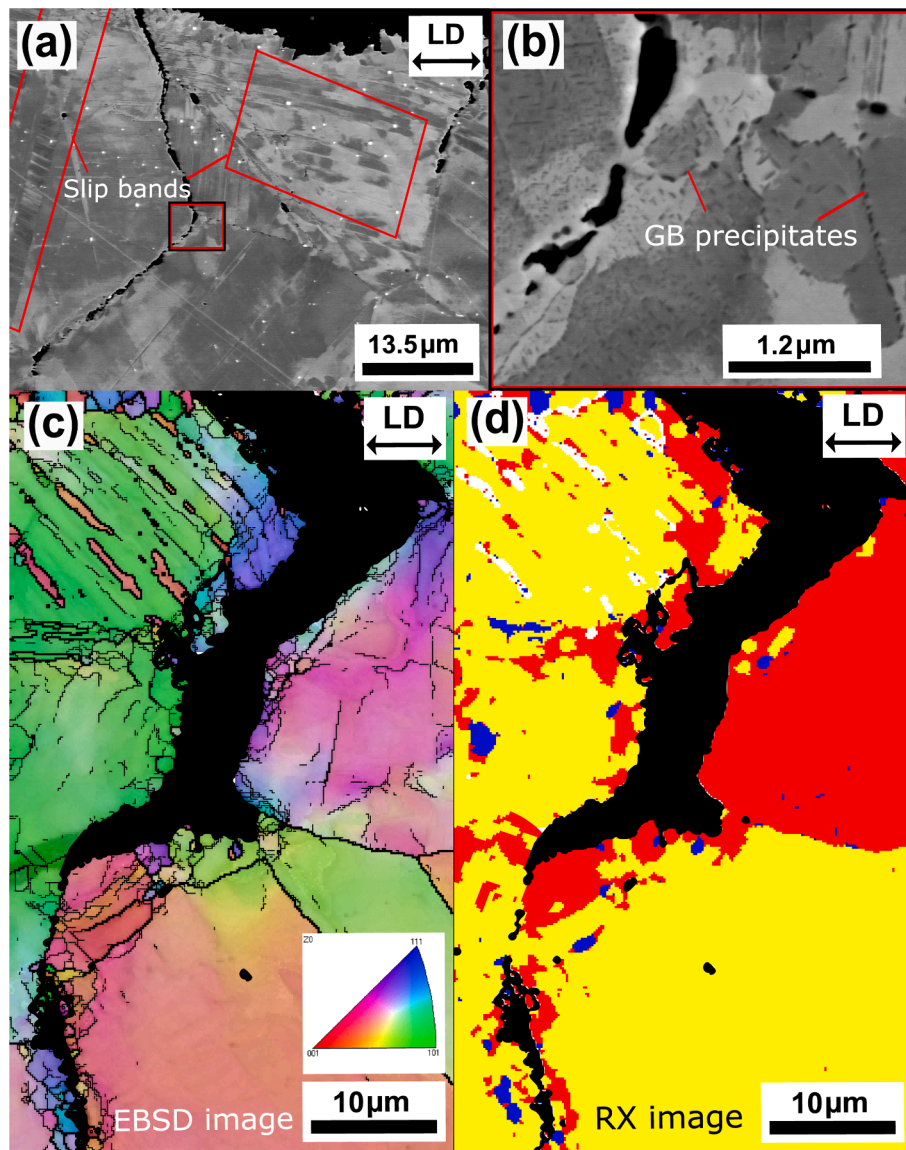


Fig. 12. Crack overview at the specimen surface of Eshete 1250, $t_d = 600$ s; (a) crack path overview, (b) zoomed in area in (a) and (c) EBSD-image of crack initiation close to the specimen surface, (d) recrystallized fraction analysis of (c).

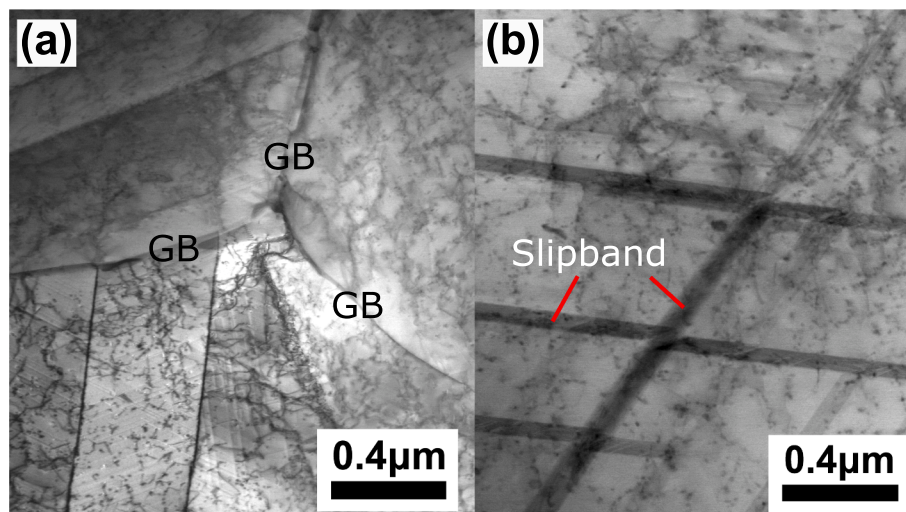


Fig. 13. STEM bright field imaging of dislocation structure for Eshete 1250, $t_d = 600$ s; (a) at a grain boundary intersection, (b) in the interior of the grain.

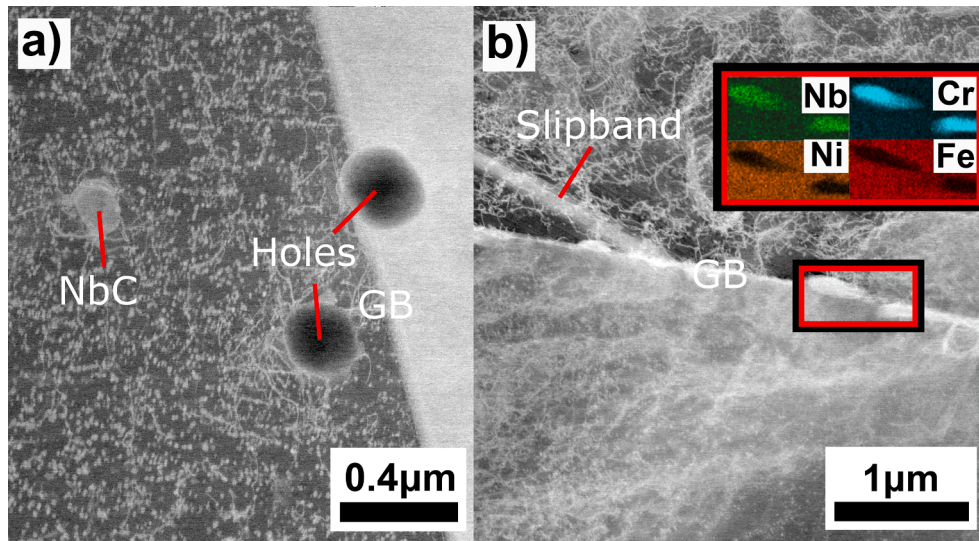


Fig. 14. STEM dark field imaging of dislocation structure and precipitate formation for Esshete 1250, $t_d = 600$ s; (a) Precipitates close to a grain boundary and the interaction with dislocations, (b) EDS-analysis of a precipitated grain boundary.

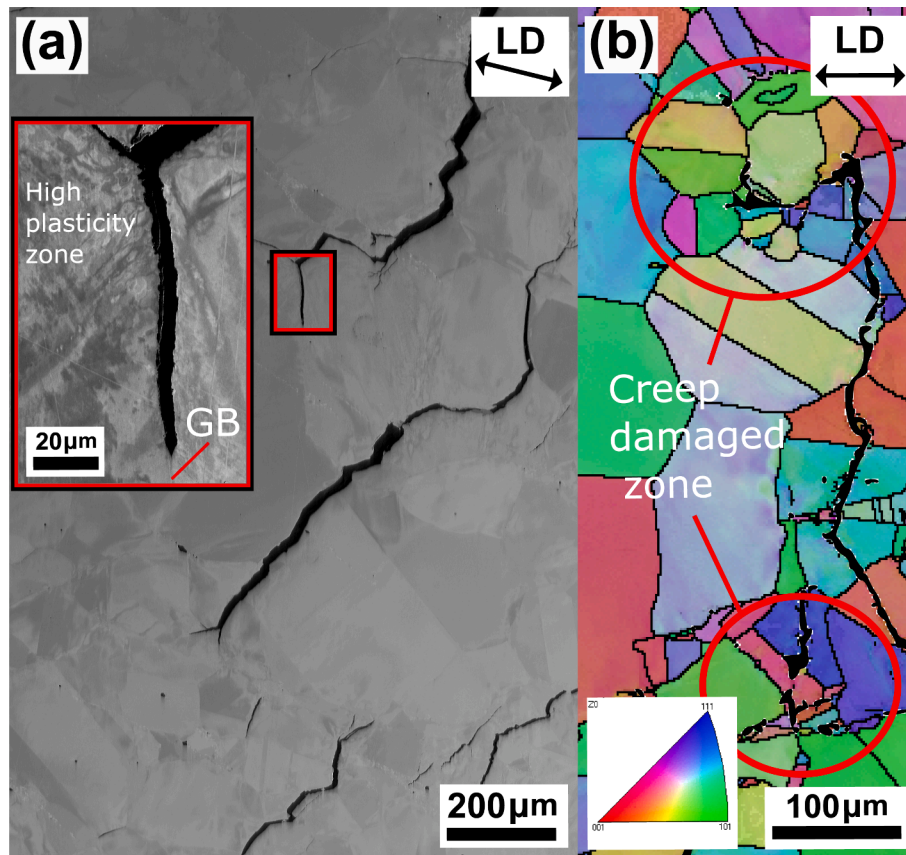


Fig. 15. Sanicro 25 microstructure, $t_d = 300$ s; (a) crack propagation overview and zoomed in area of crack junction, (b) EBSD-image of crack propagation overview.

subjected to dwell-fatigue loadings at an elevated temperature, both fatigue- and creep associated damage mechanisms seems to induce accelerated intergranular crack propagation. Therefore, it could be problematic to base the evaluation of the crack propagation only on the macroscopic analysis based on the principal cases of Hales [8] and Plumbridge [4]. This has also been discussed by Skeleton and Gandy [5].

For the Sanicro 25 tests, case 3 in Fig. 1 seems to coincide with the microstructural investigation considering the alternating intergranular

and transgranular crack propagation, where the rate of propagation is dependent on the linkage of the cracks initiated by fatigue with the intergranular creep-initiated cavities. In these areas smaller grain sizes will favour the diffusion-controlled creep mechanisms and interlinking with fatigue driven intergranular propagation is then more probable. For the transgranular propagation, smaller grain sizes are unfavourable, but with the interlinking of the creep damaged zones the overall cyclic life is decreased. This process is observed for all the investigated Sanicro

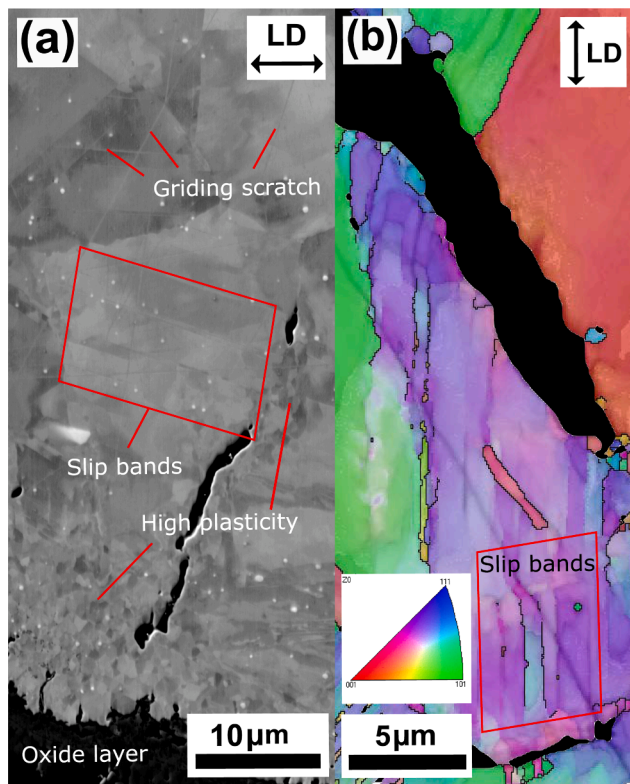


Fig. 16. Essette 1250 microstructure, $t_d = 300$ s; (a) initiation overview, (b) EBSD-image of crack initiation close to the specimen surface.

25 conditions presented in Fig. 7b, Fig. 8b and Fig. 15. The Sanicro 25 images also show areas with high plasticity associated with crack path junction, Fig. 7a or at the vicinity of the crack tip Fig. 8a. Because of the relative low stacking fault energy (SFE) of common austenitic stainless steels it is favourable to form wider stacking faults that makes cross-slips or climbing more difficult, which add to the increase of dislocation density and reduction of dynamic recovery. From the study of stacking fault energy (SFE) of different alloyed austenitic alloys by Lu et al. [23], the alloying of Sanicro 25 should render at least medium level SFE (similar to those measured in the study). This implies higher mobility of dislocations and ability for dislocations in a crystal to glide onto an intersecting slip plane easier than for the common austenitic stainless steels. In this context, considering possible DRX mechanisms that could apply for the crack tip plastic zone of Sanicro 25, discontinuous- and continuous dynamic recrystallization (DDRX and CDRX) would be up for scrutiny. From the review study of high temperature deformation of metals by Huang and Logé [24] the two mechanisms are usually most active either in low/medium SFE metals (DDRX) or in medium/high SFE metals (CDRX). The mechanism for DDRX is commonly attributed to accumulation of dislocations to a certain critical level, or critical strain, that cause DDRX nuclei groups to form by shearing/sliding of partial pre-existing grain boundaries that induce inhomogeneous local strain and bulging of serrated grain boundaries together with dislocation sub-boundaries or twins. DDRX nuclei groups are commonly observed to develop into so called "necklace structures" on the grain boundaries. Mechanisms attributed to CDRX are homogeneous misorientation increase under high temperature straining so that accumulation of dislocations progressively increase their misorientation and low angle grain boundaries (LAGBs) are created. With further straining, high angle grain boundaries (HAGBs) are formed when misorientation angles reach about 15° . However, interaction with pre-existing grain boundaries have also been described by [24] to nucleate CDRX and microshear bands is known to assist CDRX during severe plastic deformation (SPD). The DDRX mechanisms is unlikely in the case of crack tip recrystallization in

Sanicro 25 because of the transgranular cracks and no available pre-existing grain boundaries, even though the relatively low/medium SFE would suggest this. In addition, the typical necklaces structure has not been observed. According to Dong et al. [25], high temperature during testing increases the SFE which would increase dislocation mobility and the possibility for cross slip and this promotes the described mechanisms of CDRX for the crack tip plastic zone. The second phase particles of Sanicro 25 would also influence the mechanism of DRX and according to [24,26] fine dispersed dispersoids (10–300 nm) hinder boundary motion and retard recrystallization and coarse particles ($\geq 1 \mu\text{m}$) can benefit recrystallization due to large amount of stored energy in the particle plastic zone, which is termed particle stimulated nucleation (PSN). As have been presented in the result section (Fig. 9b, Fig. 10(a-b)) and in previous microstructural investigations with EDS [11], the interior of the Sanicro 25 grains consist of both coarse (Cr-carbides and Nb-carbides) and fine (coherent copper particles and Nb-carbides) second phase particles which should both influence the rate of DRX in opposite ways. Although, at high enough strain the fine particles can lose its coherency and DRX is then more probable as in the case of coherent copper precipitates studied by Miura et al. [27]. Evidently the DRX process is present in the vicinity of the magnified crack tip during the high temperature CF tests of Sanicro 25 (see Fig. 8a). The mechanism described for CDRX deemed the most reasonable to be involved during propagation of the crack and the interaction between the two damaging mechanisms, but to precisely define the process and its influence are hard without continuous examination of the crack propagation (interrupted testing) or high-resolution microscopy study of the crack tip. However from current results and discussion, the crack propagation and interaction procedure are proposed in Fig. 17: (1) A transgranular crack, originated from the surface by cracking of the oxide layer, form a plastic zone in the vicinity of the crack tip containing a region with high dislocation density. The dislocations rearrange and migrates into sub-networks to accommodate the high level of deformation (1–2). When a certain level of strain has been reached and the misorientation of the low angle grain boundaries (LAGBs) is high enough, high angle grain boundaries (HAGB) and dislocation free recrystallized grains are created (3–4). Then during the dwell time, the development of diffusion-controlled creep damage of the grain boundaries is more effective (5). The crack now propagates along with high amount of branching and the preferred path is through the creep damaged recrystallized grain boundaries (5–6). The process of 1–6 (indicated by the arrow) is then repeated for the next propagation stage of the crack (7). If a nearby area contains pre-existing creep damage, the global transgranular propagating crack will interlink with this favourable crack path and thereby adding to the overall damage and accelerate the cyclic failure (7–8). In this way the crack propagation gains its interchanging, rough and jagged nature with unambiguous crack branching, as can be seen in Fig. 7a, Fig. 8(a-c) and Fig. 15a. Observations and suggestions of similar crack propagation and recrystallization process has been presented before, but for other materials and loading conditions. For superalloys, similar recrystallized grain structures close to the main cracks were observed in [28–31] and for Kanesund et al. [28] and Kuhn et al. [29], DRX of crack tip plastic zone during thermomechanical fatigue were due to coarsening of the γ' -phase which lost its ability for pinning of the migrating boundaries. Similar loss for pinning functionality of the copper-rich precipitates and Nb-carbides of Sanicro 25 could apply in present study, where this effect only apply to the highly deformed plastic zone of the crack tip and which produce the recrystallized structure around the main cracks and not homogeneously throughout the microstructure. Furthermore, the process of DRX in the plastic zones of crack tips has also been observed for solder joints (SAC305) during thermal cycling, where strain-enhanced Ag_3Sn coalescence and facilitates recrystallization [32]. The authors suggest a crack propagation process analogous to what have been presented in this paper for Sanicro 25.

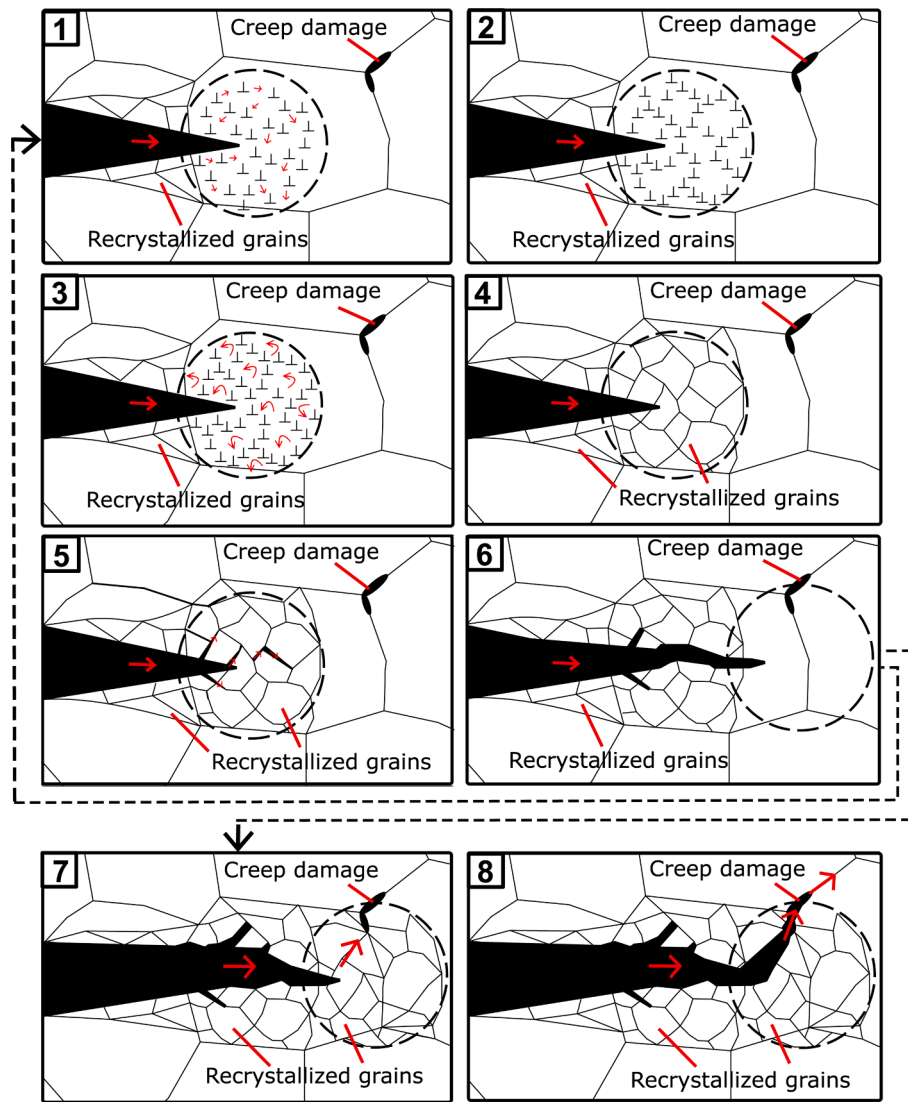


Fig. 17. Suggested schematic overview of the crack propagation and interaction process of Sanicro 25.

5. Conclusions

The microstructural evolution during high temperature cyclic loading with different dwell times of the two austenitic stainless steels, Sanicro 25 and Esshete 1250, was investigated using high-resolution microscopy techniques. The two alloys exhibit different crack propagation and creep-fatigue (CF) interaction behaviour, mainly due to the microstructural evolution during loading. The main microstructural- and CF-interaction behaviour of the two investigated alloys during the dwell-fatigue tests can be summarised as follows:

- Confirmation was found for the occurrence of coherent copper precipitates and incoherent Nb-carbides, which acted as dislocation obstacles and therefore add to the prominent hardening effect and high temperature properties of Sanicro 25 during the investigated dwell-fatigue conditions. In addition, Z-phase particles located at the grain boundaries and larger Cr-carbides were also found. Nb-carbides were also found in the Esshete 1250 microstructure, which have the same effect as for Sanicro 25, but the grain boundaries contained sparsely placed Cr- and Nb-carbides which made them more susceptible to creep damage and intergranular crack propagation.

- In contrast to the predicted cases of Hales [8], Esshete 1250 solely experienced fracture along the grain boundaries, while the interior of the grains showed high plasticity in the form of pronounced fatigue induced slip bands. The interaction of the slip bands and the grain boundaries is considered to enhance the intergranular damage process.
- The creep-fatigue interaction and crack propagation process of Sanicro 25 was proposed, which involved dynamic recrystallization (DRX) of the crack tip plastic zone. This creates high angle grain boundaries that gives an energetically privileged path of the main crack, both during the fatigue- and the dwell time part of the test cycle, which adds to the overall reduction of cyclic life in a inter-active manner.

Declaration of Competing Interest

The authors declare that they have no known competing financial interests or personal relationships that could have appeared to influence the work reported in this paper.

Acknowledgements

The present study was financially supported by AB Sandvik Materials Technology in Sweden and the Swedish Energy Agency through the Research Consortium of Materials Technology for Thermal Energy Processes, Grant No. KME-701.

References

- [1] Saidur R, Abdelaziz E, Demirbas A, Hossain M, Mekhilef S. A review on biomass as a fuel for boilers. *Renew Sustain Energy Rev* 2011;15(5):2262–89. <https://doi.org/10.1016/j.rser.2011.02.015>.
- [2] Eurelectric, Flexible generation: Backing up renewables; 2011.
- [3] Dietrich K, Latorre JM, Olmos L, Ramos A. The role of flexible demands in smart energy systems. In: *Energy Syst. Ch. Optimizati*; Springer; 2013. p. 79–97. doi: 10.1007/978-3-642-38134-8_4.
- [4] Plumbridge W. Uprating and life assessment under fatigue-creep conditions. *Int J Press Vessels Pip* 1994;59(1–3):119–29. [https://doi.org/10.1016/0308-0161\(94\)90147-3](https://doi.org/10.1016/0308-0161(94)90147-3).
- [5] Skelton R, Gandy D. Creep – fatigue damage accumulation and interaction diagram based on metallographic interpretation of mechanisms. *Mater High Temp* 2008;25(1):27–54. <https://doi.org/10.3184/096034007X300494>.
- [6] Blum R, Vanstone R. Materials development for boilers and steam turbines operating at 700 °C. In: *Proc. 6th Int. Charles Parsons Turbine Conf. Dublin, Irel*; 2003. p. 498–510.
- [7] Ogata T, Arai M. Continuous SEM observations of creep-fatigue damage processes. *Fatigue Fract Eng Mater Struct* 1998;21(7):873–84. <https://doi.org/10.1046/j.1460-2695.1998.00072.x>.
- [8] Hales R. A quantitative metallographic assessment of structural degradation of type 316 stainless steel during creep-fatigue. *Fatigue Fract Eng Mater Struct* 1980;3(4):339–56. <https://doi.org/10.1111/j.1460-2695.1980.tb01383.x>.
- [9] Jetter R. Subsection NH—class 1 components in elevated temperature service. In: *Companion guide to the ASME boiler and pressure vessel code, vol. 1, 3rd ed.* Three Park Avenue New York, NY 10016–5990: ASME; 2007. p. 409–445. doi: 10.1115/1.802694.ch12 [chapter 12].
- [10] Wärner H, Calmunger M, Chai G, Moverare J. Creep-fatigue interaction in heat resistant austenitic alloys. In: *MATEC web of conferences*; 2018. <https://doi.org/10.1051/mateconf/201816505001>.
- [11] Wärner H, Calmunger M, Chai G, Johansson S, Moverare J. Thermomechanical fatigue behaviour of aged heat resistant austenitic alloys. *Int J Fatigue* 2019;127:509–21. <https://doi.org/10.1016/j.ijfatigue.2019.06.012>.
- [12] Calmunger M, Chai G, Johansson S, Moverare J. Creep and fatigue interaction behavior in Sanicro 25 heat resistant austenitic stainless steel. *Trans Indian Inst Met* 2016;69(2):337–42. <https://doi.org/10.1007/s12666-015-0806-3>.
- [13] Chai G, Boström M, Olaison M, Forsberg U. Creep and LCF behaviors of newly developed advanced heat resistant austenitic stainless steel for A-USC. *Procedia Eng* 2013;55:232–9. <https://doi.org/10.1016/j.proeng.2013.03.248>.
- [14] He J, Sandström R, Vujic S. Creep, low cycle fatigue and creep-fatigue properties of a modified HR3C. *Procedia Struct Integr* 2016;2:871–8. <https://doi.org/10.1016/j.prostr.2016.06.112>.
- [15] Wong CY. Microstructure evolution in Nb alloyed Eshete 1250 creep resistant austenitic stainless steel. Ph.D. thesis. Swansea University; 2008.
- [16] ASTM. Standard Test Method for Creep-Fatigue Testing; 2014. doi:10.1520/E2714.
- [17] Manson SS, Halford GR, Oldrieve RE. Relation of cyclic loading pattern to microstructural fracture in creep fatigue. *NASA TM* 1984;83473.
- [18] Heczko M, Esser BD, Smith TM, Beran P, Mazánová V, McComb DW, et al. Atomic resolution characterization of strengthening nanoparticles in a new high-temperature-capable 43Fe-25Ni-22.5Cr austenitic stainless steel. *Mater Sci Eng A* 2017;719(2018):49–60. <https://doi.org/10.1016/j.msea.2018.02.004>.
- [19] Gharehbaghi A. Precipitation study in a high temperature austenitic stainless steel using low voltage energy dispersive X-ray spectroscopy [Master's dissertation]. Sweden: Royal Institute of Technology (KTH); 2012.
- [20] Sourmail T. Precipitation in creep resistant austenitic stainless steels. *Mater Sci Technol* 2001;17(1):1–14. <https://doi.org/10.1179/026708301101508972>.
- [21] Bayerschen E, McBride AT, Reddy BD, Böhlke T. Review on slip transmission criteria in experiments and crystal plasticity models. *J Mater Sci* 2016;51(5):2243–58. <https://doi.org/10.1007/s10853-015-9553-4>. arXiv:1507.05748.
- [22] Calmunger M, Chai G, Eriksson R, Johansson S, Moverare JJ. Characterization of austenitic stainless steels deformed at elevated temperature. *Metall Mater Trans A* 2017;48(10):4525–38. <https://doi.org/10.1007/s11661-017-4212-9>.
- [23] Lu J, Hultman L, Holmström E, Antonsson KH, Grehk M, Li W, et al. Stacking fault energies in austenitic stainless steels. *Acta Mater* 2016;111:39–46. <https://doi.org/10.1016/j.actamat.2016.03.042>.
- [24] Huang K, Logé RE. A review of dynamic recrystallization phenomena in metallic materials. *Mater Des* 2016;111:548–74. <https://doi.org/10.1016/j.matdes.2016.09.012>.
- [25] Dong Z, Li W, Chai G, Vitos L. Strong temperature – Dependence of Ni -alloying influence on the stacking fault energy in austenitic stainless steel. *Scripta Mater* 2020;178:438–41. <https://doi.org/10.1016/j.scriptamat.2019.12.013>.
- [26] Heidarzadeh A, Saeid T, Klemm V, Chabok A, Pei Y. Effect of stacking fault energy on the restoration mechanisms and mechanical properties of friction stir welded copper alloys. *Mater Des* 2019;162:185–97. <https://doi.org/10.1016/j.matdes.2018.11.050>.
- [27] Miura H, Tsukawaki H, Sakai T, Jonas JJ. Effect of particle/matrix interfacial character on the high-temperature deformation and recrystallization behavior of Cu with dispersed Fe particles. *Acta Mater* 2008;56(17):4944–52. <https://doi.org/10.1016/j.actamat.2008.06.012>.
- [28] Kanesund J, Moverare JJ, Johansson S. Deformation and damage mechanisms in IN792 during thermomechanical fatigue. *Mater Sci Eng A* 2011;528(13–14):4658–68. <https://doi.org/10.1016/j.msea.2011.02.063>.
- [29] Kuhn F, Zeismann F, Brückner-Foit A, Kadau K, Gravett P. Crack paths in the superalloy IN738 in aged conditions. *Eng Fract Mech* 2013;108(August):275–84. <https://doi.org/10.1016/j.engfractmech.2013.03.022>.
- [30] Ma X, Jiang J, Zhang W, Shi HJ, Gu J. Effect of local recrystallized grains on the low cycle fatigue behavior of a nickel-based single crystal superalloy. *Crystals* 9(6). doi:10.3390/cryst9060312.
- [31] Yang H, Jiang J, Wang Z, Ma X, Tu J, Shi H-J, Zhai H, et al. Fatigue fracture mechanism of a nickel-based single crystal superalloy with partially recrystallized grains at 550 °C by in situ SEM studies. *Metals* 2020;10(8):1007. <https://doi.org/10.3390/met10081007>.
- [32] Libot JB, Alexis J, Dalverny O, Arnaud L, Milesi P, Dulondel F. Microstructural evolutions of Sn-3.0Ag-0.5Cu solder joints during thermal cycling. *Microelectron Reliab* 2018;83:64–76. <https://doi.org/10.1016/j.microrel.2018.02.009>.